Deepest Limits on Scattered Light Emission from the Epsilon Eridani Inner Debris Disk with HST/STIS

P. M. Sai Krishnanth, Ewan S. Douglas, Ramya M. Anche, Justin Hom, Kerri L. Cahoy, John H. Debes, Hannah Jang-Condell, Isabel Rebollido, Bin B. Ren, Christopher C. Stark, et al.

The Astronomical Journal, 168:169 (10pp), 2024 October https://doi.org/10.3847/1538-3881/ad6efe

Deepest Limits on Scattered Light Emission from the Epsilon Eridani Inner Debris Disk with HST/STIS

Sai Krishanth P. M.[1], Ewan S. Douglas[1], Ramya M. Anche[1], Justin Hom[1], Kerri L. Cahoy[2,3], John H. Debes[4], Hannah Jang-Condell[5,6], Isabel Rebollido[7], Bin B. Ren (任彬)[8,9,10,12], Christopher C. Stark[11], Robert Thompson[1], and Yinzi Xin[2]

[1] Steward Observatory, The University of Arizona, 933 North Cherry Avenue, Tucson, AZ 85721, USA; saikrishanth@arizona.edu
[2] Department of Aeronautics and Astronautics, Massachusetts Institute of Technology, Cambridge, MA 02139, USA
[3] Department of Earth, Atmospheric, and Planetary Sciences, Massachusetts Institute of Technology, Cambridge, MA 02139, USA
[4] Space Telescope Science Institute, 3700 San Martin Drive, Baltimore, MD 21218, USA
[5] Department of Physics & Astronomy, University of Wyoming, Laramie, WY 82071, USA
[6] NASA Headquarters, Washington, DC 20546, USA
[7] European Space Agency (ESA), European Space Astronomy Centre (ESAC), Camino Bajo del Castillo s/n, 28692, Villanueva de la Cañada, Madrid, Spain
[8] Université Côte d'Azur, Observatoire de la Côte d'Azur, CNRS, Laboratoire Lagrange, Bd de l'Observatoire, CS 34229, 06304 Nice cedex 4, France
[9] Université Grenoble Alpes, CNRS, Institut de Planétologie et d'Astrophysique (IPAG), F-38000 Grenoble, France
[10] Department of Astronomy, California Institute of Technology, MC 249-17,1200 East California Boulevard, Pasadena, CA 91125, USA
[11] NASA Goddard Space Flight Center, Greenbelt, MD 20771, USA
Received 2024 February 29; revised 2024 August 9; accepted 2024 August 12; published 2024 September 23

Abstract

Epsilon Eridani is one of the first debris disk systems detected by the Infrared Astronomical Satellite. However, the system has thus far eluded detection in scattered light with no components having been directly imaged. Its similarity to a relatively young solar system combined with its proximity makes it an excellent candidate to further our understanding of planetary system evolution. We present a set of coronagraphic images taken using the Space Telescope Imaging Spectrograph coronagraph on the Hubble Space Telescope at a small inner working angle to detect a predicted warm inner debris disk inside 1″. We used three different postprocessing approaches—nonnegative matrix factorization (NMF), Karhunen–Loève Image Processing (KLIP), and classical reference differential imaging, to best optimize reference star subtraction—and find that NMF performed the best overall while KLIP produced the absolute best contrast inside 1″. We present limits on scattered light from warm dust, with constraints on surface brightness at 6 mJy as^{-2} at our inner working angle of 0.″6. We also place a constraint of 0.5 mJy as^{-2} outside 1″, which gives us an upper limit on the brightness for outer disks and substellar companions. Finally, we calculated an upper limit on the dust albedo at $\omega < 0.487$.

Unified Astronomy Thesaurus concepts: Debris disks (363); Coronagraphic imaging (313); Hubble Space Telescope (761); Exoplanet systems (484); Astronomy image processing (2306)

1. Introduction

Epsilon Eridani (ϵ Eri) (K2V; 3.2 pc; Gaia Collaboration et al. 2018) is one of the nearest solar analogs and presents an ideal laboratory for testing our understanding of debris disk formation and evolution. ϵ Eri was one of the earliest extrasolar debris disks observed, discovered by the Infrared Astronomical Satellite detection of emission in exceptional excess of what would be expected from the stellar photosphere (H. H. Aumann 1985). J. S. Greaves et al. (1998) first resolved a cold outer disk morphology at 450 and 850 μm, finding a cool, nearly face-on Edgeworth–Kuiper belt analog from 30 to 75 au. This was shown to be a uniform, circular ring using the Submillimeter Array (M. A. MacGregor et al. 2015).

ϵ Eri's infrared (IR)-excess at 24 μm (D. Backman et al. 2009) is two orders of magnitude brighter than the solar zodiacal dust (D. Backman et al. 2009; D. E. Backman & F. Paresce 1993) and may present a significant background signal, which must be overcome by future direct-imaging missions to image the nearest known giant exoplanet, ϵ Eri b (A. P. Hatzes et al. 2000).

A wide range of orbital parameters has been reported in the literature, and as observations have accumulated, the presence of this companion has become more clear. A. W. Howard & B. J. Fulton (2016) reported a "clear detection" with an eccentricity of 0.26. D. Mawet et al. (2019) performed a joint analysis of both direct-imaging nondetection sensitivity and radial velocity observations, constraining the companion parameters to a mass of $0.78^{+0.38}_{-0.12}$ $M_{\rm Jup}$ with a semimajor axis of 3.48 ± 0.02 au and a nearly circular orbit ($e = 0.07^{+0.06}_{-0.05}$). S. Hunziker et al. (2020) observed ϵ Eri with the SPHERE ZIMPOL instrument with the VBB filter (broadband Vis-NIR filter at 735 nm). By combining polarimetric and angular differential imaging, they placed 1σ limits on the polarized intensity approaching contrasts of 10^{-8} at 1″ separation and 0.5-1e-7 sensitivity to unpolarized point sources at 1″. J. Llop-Sayson et al. (2021) applied ground-based direct-imaging nondetection limits, radial velocity, and astrometric constraints to find a lower mass $0.66^{+.12}_{-.09}$ and a relatively high inclination $i = 78.81^{+29.34}_{-22.41}$. G. F. Benedict (2022) reanalyzed Hubble Fine Guidance Sensor (FGS) astrometry observations (G. F. Benedict et al. 2007) in the context of these new observations and found $i = 45 \pm 8$. Additionally, the $42.7^{11}_{9.5}$ degree obliquity between the resolved outer debris disk(s) and the star (S. A. Hurt & M. A. MacGregor 2023) suggests ϵ Eri may

[12] Marie Skłodowska-Curie Fellow.

Table 1
Summary of Observations Made with Our GO 15217 Program

Visit	Target	Start Time (UT)	Roll Angle (deg)	Subpixel Dithering (pix)	Exposure time (s)	N_{images}	GS Acquisition
V-I-4	ϵ Eri	2018-11-28 06:58:49	206.33	−0.25	83.99	31	GSFAIL
V-I-4	ϵ Eri	2018-11-28 07:13:15	206.33	0	98.29	31	GSFAIL
V-I-4	ϵ Eri	2018-11-28 07:27:55	206.33	+0.25	83.99	31	GSFAIL
V-I-5	ϵ Eri	2018-11-28 08:34:10	191.33	−0.25	83.99	31	GSFAIL
V-I-5	ϵ Eri	2018-11-28 08:48:36	191.33	0	98.29	31	GSFAIL
V-I-5	ϵ Eri	2018-11-28 09:03:16	191.33	+0.25	83.99	31	GSFAIL
V-I-8	δ Eri (PSF)	2018-11-28 10:10:09	200.89	−0.25	71.30	32	OK
V-I-8	δ Eri (PSF)	2018-11-28 10:24:28	200.89	0	83.70	32	OK
V-I-8	δ Eri (PSF)	2018-11-28 10:38:58	200.89	+0.25	71.30	32	OK
V-I-6	ϵ Eri	2018-11-28 11:44:51	176.33	−0.25	83.99	31	GSFAIL
V-I-6	ϵ Eri	2018-11-28 11:59:17	176.33	0	98.30	31	GSFAIL
V-I-6	ϵ Eri	2018-11-28 12:13:57	176.33	+0.25	83.99	31	GSFAIL
V-II-1	ϵ Eri	2018-12-27 16:33:53	221.33	0	233.50	95	OK
V-II-2	ϵ Eri	2018-12-27 19:44:35	236.33	0	233.50	95	OK
V-II-3	ϵ Eri	2018-12-27 18:09:59	251.33	0	233.50	95	OK
V-II-7	δ Eri (PSF)	2018-12-27 21:19:57	229.02	0	200.99	99	OK

Note. GSFAIL indicates observations where the FGS was unable to lock on to more than one guide star, leading to a higher rate of pointing drift than nominal.

have a formation history significantly different from the Solar System and that the inner disk's inclination is far from certain.

Scattered-light imaging efforts to resolve questions about the location, composition, and orientation of the debris around ϵ Eri have proven unsuccessful. A search by C. R. Proffitt et al. (2004) with the Space Telescope Imaging Spectrograph (STIS) put a limit of 0.378 μJy/arcsecond^2 for scattered light from the outer ring. And most recently, S. G. Wolff et al. (2023), using STIS, placed a constraint of 4 μJy/arcsecond^2 at radial separations outside 10″.

Combining new observations with nonnegative matrix factorization (NMF) point-spread function (PSF) subtraction, this work will present new limits on the broadband unpolarized scattered light from extended and point sources around ϵ Eri using the STIS instrument aboard Hubble Space Telescope (HST). In Section 2, we describe the observation program used to collect data using the WEDGE A 1.0 occulter position, and in Section 3, we present our reduction strategy, with NMF being our primary method of postprocessing. In Section 4, we summarize our results, including a new contrast floor, and describe the PSF color mismatch problem that affects classical reference differential imaging (RDI) subtraction with STIS. Finally, in Section 5, we discuss future observatories and their ability to directly image the ϵ Eri inner disk in scattered light. We also compare our different postprocessing methods and present some extensions of our NMF reduction.

2. Observations

We observed ϵ Eri with the HST STIS WEDGE A 1.0 coronagraph (C. A. Grady et al. 2003) using the 50CORON aperture (central wavelength of 5743.706 Å with a wavelength range from 1640 Å to 10300 Å; full width half maximum (FWHM) = 4333 Å) with 1024 × 110 pixel frames to minimize readout time and a gain of 4 e$^-$/ADU. Our observations were part of HST cycle 25 observations (PID 15217). Exposure times of 2.3 s were set to prevent saturation at the inner working angle by comparison with other STIS coronagraph observations. Observations were carried out in two campaigns, the first visit (V-I) on 2018 November 28 starting at 06:53:59 UTC and a second visit (V-II) on 2018 December 27 starting at 16:28:59 UTC. V-I and V-II included three orbits of ϵ Eri, each at a different roll angle separated by 15°, and one orbit of reference star Delta Eridani (δ Eri). A summary of these observations is shown in Table 1 and the corresponding combined visits from these observations are shown in Figure 1.

δ Eri, a K0+IV star 9 pc distant, was chosen because of excellent color matching (the B-V color differs from ϵ Eri by only 0.04 mag), proximity on the sky minimizing thermal changes, and lack of known circumstellar material. δ Eri exposure times were decreased to 1.9 s to provide comparable counts per frame; this is done in part to mitigate differences in PSF shape due to charge transfer inefficiency. Even at high count rates where little residual charge is lost, differences at the 10^{-8} contrast level are possible if the count rates on the STIS CCD differ by more than a factor of a few (J. H. Debes et al. 2019). V-I was designed to maximize PSF library matching using subpixel dithering, with 3 pointings across the mask separated 0.25 pix, which has previously shown promising results with the BAR5 coronagraph (J. H. Debes et al. 2019).

In 2018 October, Gyro 2 on HST failed and was replaced with Gyro 3. Gyro 3, with a higher level of rate bias shifts than previous HST Gyros, made target acquisitions fail at a higher than historical rate. For visit V-I, the fine guidance sensor was only able to acquire on a single guide star, causing a slow drift to the stellar pointing over the course of each visit and enhancing the overall level of jitter (average $\sigma = 10.5$ mas over an orbit). The drift itself was not sufficient to render the observations unusable but decreased the similarity between observations and the past observations used to generate the reference library. HST pointing jitter, in particular, can impact contrast at small inner working angles (J. H. Debes et al. 2019).

For V-II, subpixel dithering was removed from the program and three additional roll angles were observed along with a second observation of δ Eri. The target acquisition for these visits was nominal, and the jitter level, as measured by the stellar centroids was slightly improved over V-I (average $\sigma = 9$ mas over an orbit). The total roll angle space spanned was 75°, from 176°.33 to 251°.33 in HST V-3 roll coordinates. The total integration time was 1507 s on ϵ Eri and 455 s on δ-Eri.

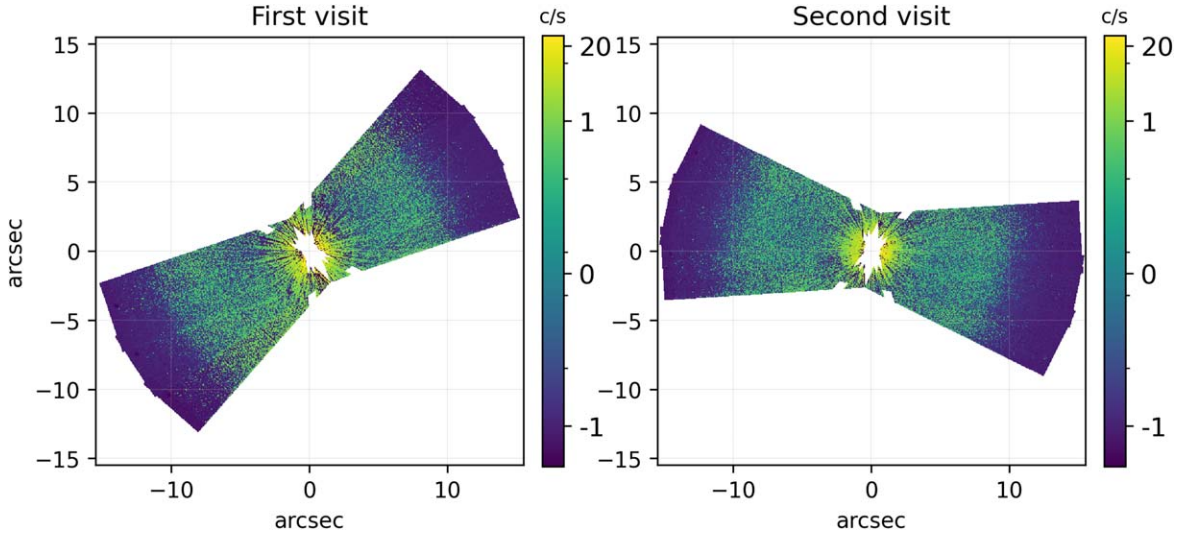

Figure 1. Median combined images for each visit. The mean of the median of each roll for the first and last visit shows relatively similar structure and brightness between the two visits. No images were dropped before the median combining shown in this illustration.

3. Reduction

3.1. Preprocessing

We obtained raw and uncalibrated STIS WEDGE A 1.0 images from the MAST[13] archive. Following S. G. Wolff et al. (2023), we used the AUTOFILET package (R. A. Jansen et al. 2003) to remove the readout video noise present in all CCD side 2 observations since 2001. The video noise-removed raw frames were processed through the standard calstis pipeline,[14] yielding dark and bias-subtracted flat-fielded frames. Coronagraphic flats were not needed as the flux error due to differences in the flat field across the image is less than 2% and impacts both the target and reference stars equally. We constructed an algorithmic masking function for the occulting wedge of the coronagraph and the diffraction spikes produced by it. The central wedge mask had a FWHM of 1.″1 while the masked diffraction spikes had a thickness of 0.″7. We then checked every frame by eye to ensure mask efficacy, ensuring minimal loss of scientific information. We find significant improvement in contrast performance with well-masked frames, with higher recovery of data behind the mask, and prevention of overfitting during postprocessing. Our data reduction from this point follows the STIS coronagraph pipeline described in B. Ren et al. (2017).

3.2. Postprocessing

We undertook three postprocessing approaches, classical PSF subtraction, Karhunen–Loève Image Processing (KLIP; A. Amara & S. P. Quanz 2012; R. Soummer et al. 2012), and NMF (B. Ren et al. 2018). A library of STIS WEDGE A 1.0 images of δ Eri was used to produce a RDI PSF library for all three postprocessing approaches applied, totaling 380 individual reference readout images.

3.2.1. NMF

Our NMF implementation is described in detail in B. Ren et al. (2018) and P. M. Sai Krishanth et al. (2023). We use 90% of the nearest reference images in correlation—342 frames—to model the target images with 30 NMF components. By inspection, we found a minor increase in contrast when using 30 components over 10, but larger numbers of components did not yield a significant improvement in contrast. After NMF-mode subtraction, we applied 3σ clipping around the data median to every frame. The frames were then rotated into sky coordinates (north up, east left) and cropped to 600×110 pixels. Due to the combination of pointing offsets and the lack of FGS lock, some frames were significantly off the coronagraphic wedge and were poorly subtracted. These frames were removed by sorting the post-subtraction frames by the standard deviation of the cropped residual images and discarding the 10% of frames with the highest standard deviation. The remaining frames were median combined to produce a final image, as shown in Figure 2.

3.2.2. KLIP

To assess the sensitivity of our observation to substellar companions, we perform PSF subtraction using KLIP (R. Soummer et al. 2012), with `pyKLIP` (J. J. Wang et al. 2015) using a large number of logarithmically spaced concentric annular search zones further divided into four subsections and a range of Karhunen–Loève (KL) modes up to 100. Having "aggressive" parameters such as larger numbers of annuli and KL modes will lead to higher contrast overall. This is ideal for detecting point sources such as companions but leads to significant over-subtraction of extended structures such as disks (R. Soummer et al. 2012). We preferentially order frames in the RDI PSF library by calculating a correlation matrix of all science frames and reference frames, similar to KLIP-RDI approaches performed in G. Duchêne et al. (2020) and C. Chen et al. (2020). Further calibration of the contrast curves measured from the reduced KLIP images is performed by injecting fiducial point sources with known fluxes into the pre-processed data set at varying separations and position angles. We then perform a KLIP-RDI reduction with the same parameters as the initial reduction. The fluxes from the injected planets are retrieved to assess the throughput of the KLIP reduction, which is then used to calibrate the initial contrast measurement. After exploring the parameter space of different numbers of annuli and KL modes, we chose a combination of 50 annuli and 10 KL modes to

[13] https://mast.stsci.edu/
[14] https://stistools.readthedocs.io/en/latest/calstis.html

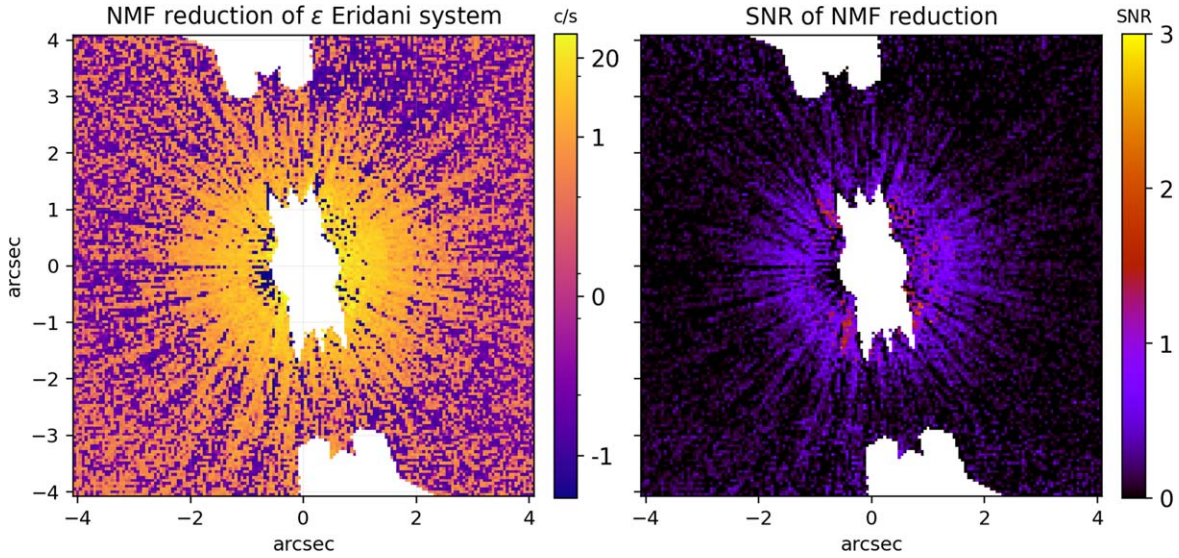

Figure 2. Left panel: NMF result using 90% closest frames of δ Eri as reference and 30 NMF components. Right panel: signal-to-noise ratio (SNR) map of the reduced image, calculated by dividing the median of used frames by the standard deviation of the used frames.

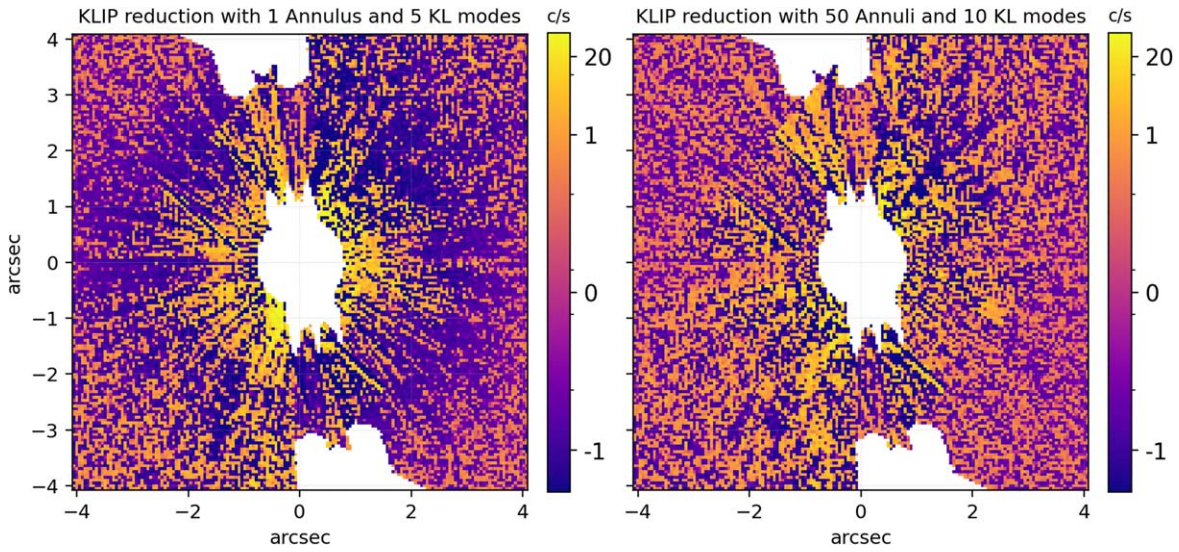

Figure 3. Left panel: disk-optimized KLIP reduction. The combination of a single annulus and a low number of KL modes is ideal to avoid oversubtraction and preserve the disk signal. Right panel: KLIP reduction optimized for detection of substellar companions. This combination of a large number of annuli gives us the most contrast while 10 KL modes give us a good balance of contrast and throughput.

optimize our KLIP reduction for substellar companions. We also performed a disk-optimized KLIP reduction using one annulus and five KL modes. We use a single annulus for more continuous flux profiles in extended sources, and five KL modes to avoid significant oversubtraction and preserve disk throughput at the expense of lower contrast. The final median combined images of both these reductions are shown in Figure 3.

3.2.3. Classical RDI

We conducted a classical RDI reduction of the data using the two orbits targeting δ Eri as the sole reference star and largely following the same procedure detailed in G. Schneider et al. (2014) and J. H. Debes et al. (2019). Each frame estimated the stellar centroid behind the mask by calculating the intersection of the diffraction spikes, and through subpixel interpolation rectified to a common center (G. Schneider et al. 2014). Differential offsets and scalings between the PSF reference and the target were performed for each orbit, using a mask to occult pixels impacted by the wedge and diffraction spike residuals. The individual orbits were rotated to the proper position angle on the sky and combined into a final subtracted image. This procedure was done for both short exposure times and long exposures at the end of each visit. Both the long and short exposure subtractions were combined into a final image presented in Figure 4.

4. Results

4.1. Evaluating Contrast

To convert to relative contrast values, we used the HST Exposure Time Calculator[15] to find the global source electron rate (914,424,193 [e/s]) for a $V = 3.72$ mag K2V star

[15] http://etc.stsci.edu/etc/input/stis/imaging/

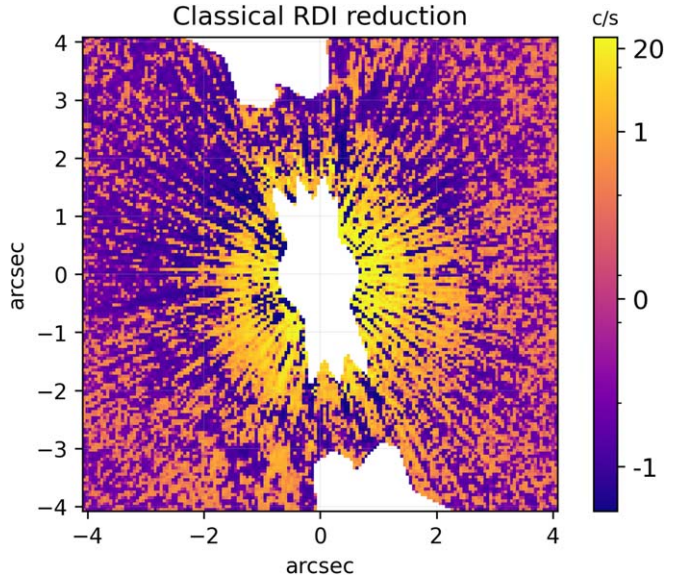

Figure 4. Classical RDI subtraction as described in 3.2.3.

(A. J. Pickles 1998). We used this value instead of the "peak pixel" value to account for the quantum yield correction at shorter wavelengths. The electron rate is converted to counts assuming the nominal gain of 4.087 electrons/DN, for a DN rate of 2.24E8 [ct s^{-1}]. Following S. G. Wolff et al. (2023), we chose to calculate contrast using median absolute deviation (MAD) over standard deviation. As noted by S. G. Wolff et al. (2023), MAD is a better estimator for smaller data sets, being more robust to outliers. We determined the MAD value in 1 px wide annuli centered around ϵ Eri using the *radial_profile* function in the package Physical Optics Propagation in Python (poppy; M. D. Perrin et al. 2012). We divided our processed images by the peak pixel value to calculate image sensitivity in contrast units. To convert the sensitivity to surface brightness (in mJy $arcsec^{-2}$), we adopt the conversation factor for a spectrally flat source of 0.1765 mJy $arcsec^{-2}$ per count per second from previous studies G. Schneider et al. (2014; their Table 4). We present contrast curves in Figures 5 and 6. In Appendix B, we further investigate the residuals remaining after PSF subtraction to quantify the upper limit on detected flux. Consistent with Figure 2, we find that our measured flux residuals are consistent with zero at all separations.

4.2. Upper Limits on Disk Brightness

While we were not able to resolve the inner disk, we can place constraints on the surface brightness with the deepest observed contrast floor in scattered light. At the inner working angle of 0.″58, we note an upper limit on the surface brightness of 5.98 mJy $arcsec^{-2}$. Additionally, outside 1″, we place an upper limit of 0.57 mJy $arcsec^{-2}$. Since the inner disk is expected to be at or under 1″ in diameter (D. Backman et al. 2009; K. Y. L. Su et al. 2017), this allows us to place an upper limit on the surface brightness of the inner disk. We note that the upper bound placed on disk flux in this work is lower than similar limits established in S. G. Wolff et al. (2023), particularly while employing NMF. The improvement in contrast is attributable to an increase in the number of components used during NMF, and to a larger extent uniform sigma clipping across all postprocessing methods. In Appendix A, we also place upper limits on planetary mass using the SonoraBobcat models (M. S. Marley et al. 2021).

5. Discussion

5.1. Placing New Limits in Context

We are able to better constrain the dust properties of the ϵ Eri system based on the new surface brightness limits established in this work. Using the fractional luminosity value for the inner disk from D. Backman et al. (2009; their Table 2), we place an upper limit on the dust albedo of $\omega < 0.487$, using Equation (5) from É. Choquet et al. (2018),

$$\omega = \frac{f_s}{f_e + f_s} \tag{1}$$

where $f_s = 3.136 \times 10^{-5}$ is $\mathrm{Flux_{dust}}/\mathrm{Flux_{star}}$ in the STIS bandpass and $f_e = 3.3 \times 10^{-5}$. To further place our surface brightness results in context, we make use of models generated by the radiative transfer software MCFOST (C. Pinte et al. 2006), including extensive work done by S. G. Wolff et al. (2023), S. Ertel et al. (2020), and D. Backman et al. (2009).

We first used the IRS best-fit parameters, that better fit the inner disk, from S. G. Wolff et al. (2023), to generate an MCFOST model resembling the structure proposed by D. Backman et al. (2009). This model has an upper limit of $10^{-7}(M_\oplus)$ in dust mass within 3 au of ϵ Eri and a minimum grain size, $a_{\min}$=0.5 μm. We find that this model predicts a surface brightness of 0.012 mJy $arcsec^{-2}$ at 1″, which is well below our sensitivity of 0.5 mJy $arcsec^{-2}$ at 1″. To further place this model in the context of STIS sensitivity, we used an expression from J. H. Debes et al. (2019) to predict contrast across significantly longer integration times. We found that an integration time of 26.67 hr (i.e., extrapolating to the contrast that could be achieved with a STIS program if we use integration times similar to the Nancy Grace Roman Space Telescope) would yield an improvement of ∼4.6 times what we achieved in our program. Accounting for this, we can predict a theoretical surface brightness of 0.11 mJy $arcsec^{-2}$ achievable by STIS at 1″, which is still an order of magnitude larger than the brightness predicted by the model informed using parameters from S. G. Wolff et al. (2023).

We also consider an alternate model informed by the HOSTS survey, carried out using the Large Binocular Telescope Interferometer (LBTI). S. Ertel et al. (2020) provide a disk flux estimate of 296 ± 55.6 zodis in the conservative aperture of 27 pixels radius with a scale of 17.9 mas $pixel^{-1}$. Following the procedure in (S. Ertel et al. 2020), we calculated the flux for ϵ Eri in the *N* band to be 9325 mJy. Using MCFOST, we then generated a smooth disk model extending to 1″ with a single power law ($\alpha = -0.45$) using Mie grains of dust mass $1.145 \times 10^{-9}(M_\oplus)$, to agree with the estimated flux from the HOSTS detection. In the HST bandpass, this yields a disk brightness < 0.1 mJy $arcsec^{-2}$ outside of 0.″5, which is below our detection limit.

5.2. Comparison of Postprocessing Approaches

NMF iteratively decomposes the observed PSF into a positive, nonorthogonal set of instrumental PSF basis modes, which avoids the oversubtraction found in the principal component analysis family of modeling approaches such as KLIP. In contrast to KLIP, NMF components are sparse and smaller in magnitude, which leads to less overfitting in the modeling stage, and thus less oversubtraction. NMF also maximizes throughput for extended sources at the expense of

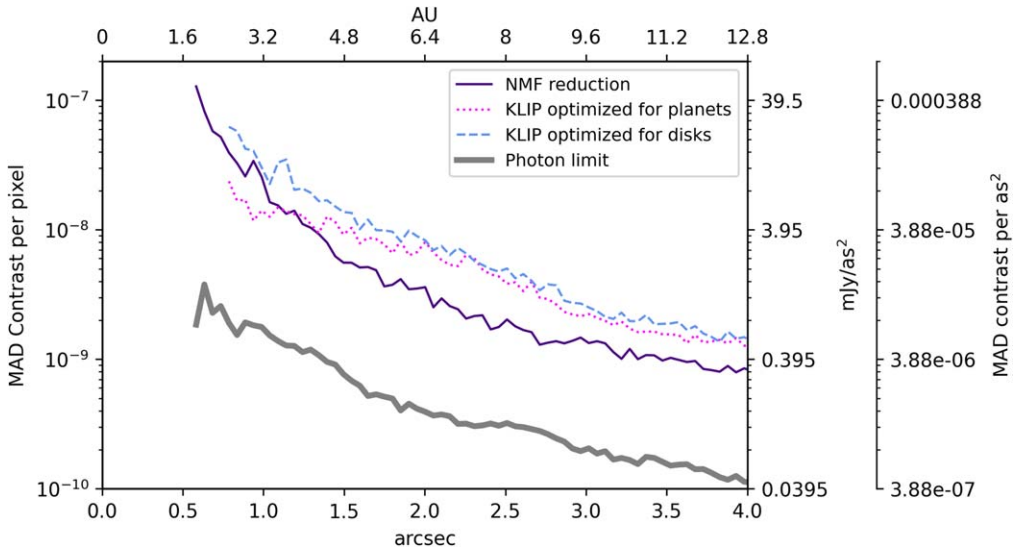

Figure 5. Contrast vs. separation sensitivity curves showing the KLIP reduction optimized for disks (in dashed blue), KLIP reduction optimized for planets (in dotted magenta), NMF reduction (in solid purple), and the photon limit (in thick solid gray). We note that the KLIP subtraction optimized for planets has the best contrast under 1″, but the NMF curve has the best contrast overall.

some point-source sensitivity and allows us to directly establish a contrast floor and avoid the uncertainty of forward-modeling hypothetical disk geometries to establish a detection limit. In this work, we find that NMF has the best disk-focused contrast performance, giving us a contrast of 1.48×10^{-8} (corresponding to a surface brightness of 0.59 mJy arcsec^{-2}) at 1″.

On the other hand, using KLIP provides superior absolute contrast for point sources but suffers from self-subtraction effects, particularly for face-on extended sources. Thus, we performed two KLIP subtractions: one focused on an extended source, and one focused on a point source. We find that the disk-focused KLIP reduction gives us a contrast of 2.25×10^{-8} (corresponding to a surface brightness of 0.89 mJy arcsec^{-2}) at 1″. The planet-focused KLIP reduction gives us the best overall contrast of 1.26×10^{-8} (corresponding to a surface brightness of 0.5 mJy arcsec^{-2}) at 1″. The disk-optimized KLIP contrast curve (Figure 5) has a slightly worse contrast performance than presented since we calibrated our contrast curve by injecting planetary companions. With performance already worse than NMF, we elected to not recalibrate by injecting a disk model because that would result in worse performance regardless of the model used.

We also present a classical RDI subtraction approach, i.e., subtracting the PSF of the reference from the PSF of the target, as a baseline for comparison against NMF and KLIP. We find that classical RDI has the worst contrast performance of the three postprocessing approaches used in this paper. We achieve a contrast of 4.47×10^{-8} (corresponding to a surface brightness of 0.89 mJy arcsec^{-2}) at 1″.

5.3. NMF Using a Broader PSF Library

Building upon the analysis presented in P. M. Sai Krishanth et al. (2023), we also investigated the contrast limits that could be achieved using the entire STIS library of frames as our RDI PSF library, totaling 4796 frames. To produce this curve, we used 90 components constructed from the 10% closest reference frames, calculated using the Euclidean norm. Excluding δ Eri from the library leads to an order of magnitude worse contrast performance compared to our NMF curve produced using only δ Eri. We note, however, that at lower angular separations, it closely approaches the classical RDI curve. We posit that in the absence of a good reference source, this is a viable approach to performing RDI on a disk-specific data set. We also postulate that this contrast performance could be improved with better masking of the diffraction spikes produced by the STIS coronagraph. Currently, masking is done manually on a frame-by-frame basis, and the number of individual frames using the WEDGE A 1.0 occulter position (4796 frames) makes this an untenable approach. Previous approaches to using an entire instrument archive to build a PSF library to perform RDI used a simpler mask (C. Xie et al. 2022) with better results. We also constructed another library with the entire library of frames (including δ Eri) and found that the contrast performance was identical to using δ Eri alone. This was expected since δ Eri constituted most of the closest frames selected by the Euclidean norm measure. We can compare our results to a similar RDI analysis of the SPHERE archive performed by C. Xie et al. (2022), but are unable to reproduce their finding where they show that more references in the library lead to better subtractions overall. This is not surprising, however, given the differences in instruments; the STIS CCD is very sensitive to variations in stellar chromaticity. We therefore elected to use only δ Eri as our source to perform RDI to save on computational resources.

5.4. Current and Future Observations of ϵ Eri

Although we were unable to resolve the inner disk, current and upcoming instruments will likely be able to resolve the disk components of ϵ Eri in both scattered-light and mid-IR thermal emission.

The ϵ Eri system is planned to be observed by the James Webb Space Telescope (JWST), using both the Mid-Infrared Instrument (MIRI) and the Near-Infrared Camera (NIRCam) instruments (GTO 1193). The MIRI observations are primarily aimed at thermally imaging the outer rings and structures affected by scattered light while the NIRCam observations aim

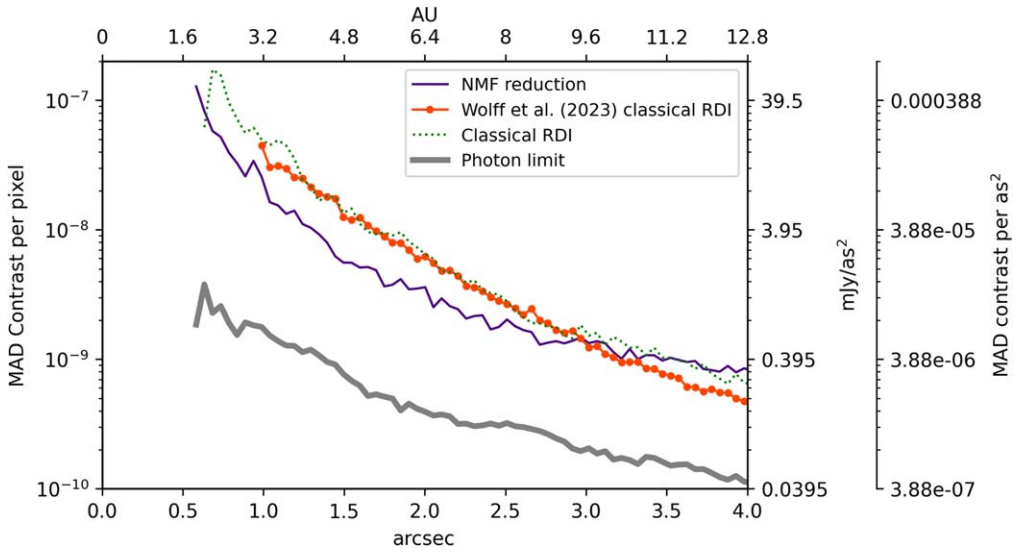

Figure 6. Contrast vs. separation sensitivity curves showing our classical RDI (in dotted green), classical RDI reduction from S. G. Wolff et al. (2023; in dotted–dashed orange), NMF reduction (in solid purple), and the photon limit (in thick solid gray). We note that the NMF curve has better contrast out to 3″, after which both classical RDI reductions perform better. Our reductions also extend to a smaller radial separation because of the occulter location we used in our observations.

Table 2
Summary of Disk Properties used in Modeling the Ertel (S. Ertel et al. 2020), Backman (D. Backman et al. 2009), and Wolff (S. G. Wolff et al. 2023) Models using MCFOST

	Ertel (2020)	Backman (2009)	Wolff (2023)
Dust morphology	Continous	Ring	Ring
Disk extent (au)	0.1–3	3	0–3
Dust Mass ($M_\oplus$)	1.149×10^{-9}	1.80×10^{-7}	9.81×10^{-8}
Minimum grain size-$a_{\rm min}$(μm)	0.1	3	1
Maximum grain size-$a_{\rm max}$(μm)	1000	3	10000
Power law of grain size distribution	3.65	3.5	3.5
Grain composition	100% astrosilicates	100% astrosilicates	60% astrosilicates 40% organic refractory material
Surface density exponent	-0.45 (α)	5 ($\alpha_{\rm in}$), -5 ($\alpha_{\rm out}$)	5 ($\alpha_{\rm in}$), -5 ($\alpha_{\rm out}$)

Note. The models generated using these properties were then propagated through the Roman Coronagraph. The grain composition for the Wolff model was obtained from N. P. Ballering et al. (2016).

to search for massive planets at both a small Inner Working Angle (IWA; 0.″64) and large Outer Working Angle (OWA; up to 2.″2). These observations will likely resolve warm asteroid belt analogs around ϵ Eri and further our understanding of small grains that contribute to the halo around the system. These observations can potentially provide the first resolved constraints on the disk morphology.

The Nancy Grace Roman Coronagraph Instrument, expected to be launched in 2027, will facilitate scattered-light observations of fainter debris disks (reaching a contrast $\sim 10^{-8}$) and probe the dust closer ($\sim$1 au) to the nearby stars (N. J. Kasdin et al. 2020; I. Poberezhskiy et al. 2021, 2022). The Roman Coronagraph supports narrow field observations with the hybrid Lyot coronagraph (HLC) at 575 nm and wide-field observations with the shaped pupil coronagraph (SPC) at 825 nm. As the Roman Coronagraph will be able to probe smaller angular separations with higher contrast than previously achievable, it is expected to detect the scattered light from the unresolved inner disk of ϵ Eri. To simulate observations of the inner ϵ Eri debris ring through the Roman Coronagraph, we first create disk models using the radiative transfer software MCFOST (C. Pinte et al. 2006). We generated disk models informed by the properties determined in D. Backman et al. (2009), K. Y. L. Su et al. (2017), S. G. Wolff et al. (2023), and LBTI HOSTS measurements (S. Ertel et al. 2020). The models using the Mie (compact spherical) grains estimate a disk brightness much greater > 0.5 mJy arcsec^{-2} outside of 1″ for D. Backman et al. (2009) and S. G. Wolff et al. (2023), and could have been easily detected in our HST observations. Thus, we created two ring models with properties from D. Backman et al. (2009) and S. G. Wolff et al. (2023) using distributed hollow spheres grains where the disk brightness is $\sim$0.3 mJy arcsec^{-2} (disk properties provided in Table 2) and one smooth disk model, informed by the LBTI HOSTS measurements from S. Ertel et al. (2020). Since the observed brightness of an IR-excess inferred disk is highly degenerate with grain properties and geometry, we scaled the disk brightness by 0.168 mJy arcsec^{-2} for all the models to the contrast level of 2×10^{-8} derived from NMF reduction contrast curve shown in Figure 6.

We simulate the S. Ertel et al. (2020) model through the HLC mode and D. Backman et al. (2009) and S. G. Wolff et al. (2023) models through the SPC mode of the Roman

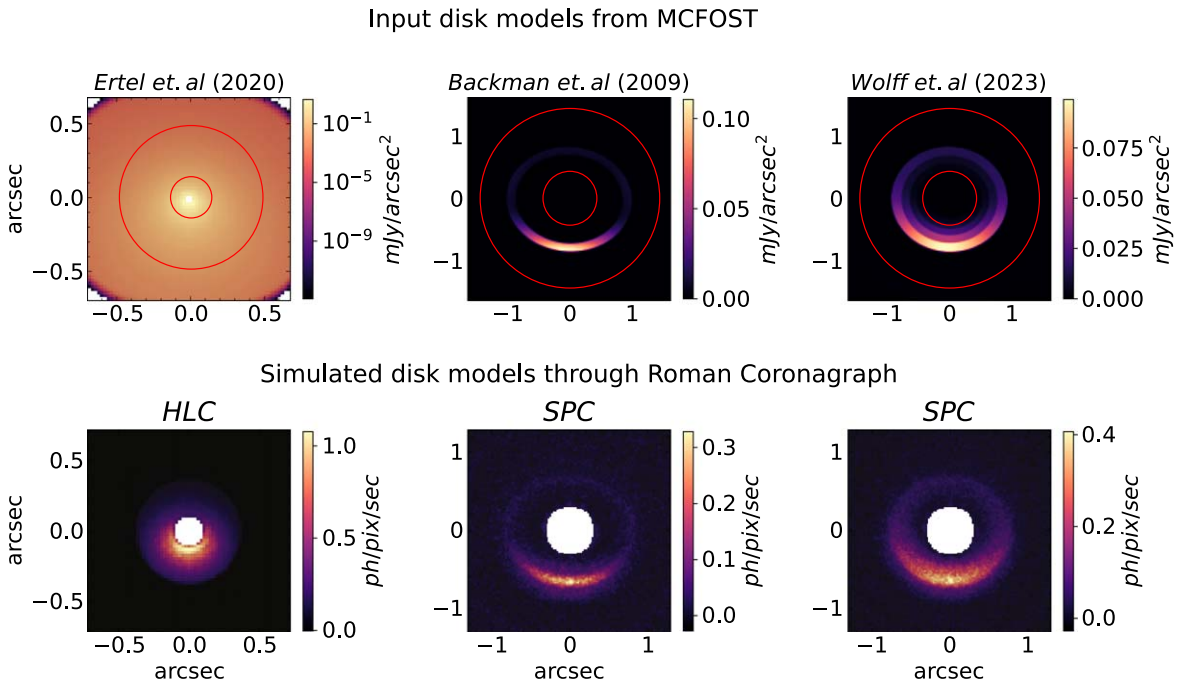

Figure 7. The simulated disk models of ϵ Eri through the Roman Coronagraph Instrument. We use the LBTI HOSTS measurements from S. Ertel et al. (2020) for the smooth disk model and disk properties from D. Backman et al. (2009), and S. G. Wolff et al. (2023) for the two ring models. The disks are processed through the HLC and SPC mode of the Roman Coronagraph instrument using realistic noise and speckle background levels from OS9 (for HLC) and OS11 (for SPC) for a 26.67 hr exposure. The IWA and OWA for the coronagraphs are marked in red for each of the input disk models. The Roman Coronagraph will achieve deeper contrast at smaller separations with both modes than we have achieved with STIS.

Coronagraph as the ring models fall outside the OWA of the HLC mode. We incorporated various noise factors from jitter, speckles, and the EMCCD (B. Nemati et al. 2020) using the "OS9"[16] and "OS11"[17] simulations for HLC and SPC modes, respectively. The various steps involved in the simulation process are explained in more detail in R. M. Anche et al. (2023). The input disk models and the corresponding simulated output disk models are shown in Figure 7. As shown in the lower panel of Figure 7, the inner dust ring around ϵ Eri is detectable in scattered light with both modes of the Roman Coronagraph, depending on the true size/density distribution of the disk. We note the exposure time of these Roman simulations is 26.67 hr versus the approximately 0.5 hr integration time here (see Section 5.1); however, the optimized Roman coronagraphs are expected to have a much lower photon noise limit and to be insensitive to stellar color mismatch (M. Ygouf et al. 2021).

6. Summary

We have presented new limits on the surface brightness in scattered light of an inner debris disk around the ϵ Eri system using the STIS coronagraph on HST. To achieve a small IWA, we used the WEDGE A 1.0 occulter location on the coronagraph and observed an effective IWA of 0.″58. Although most of our observed ϵ Eri frames had the telescope unable to successfully achieve FGS lock, we account for these "bad frames" by calculating the standard deviation of all observed frames and discarding the worst 10%. We applied three postprocessing approaches; NMF, KLIP, and classical RDI to attempt imaging the disk and achieve the highest possible contrast. Of these approaches, we find that NMF gave us the best contrast performance for an extended source. We observed that an extension of our NMF reduction approach by using the entire library of STIS coronagraphic frames had negligible impact on final contrast while using a library without any direct reference observations also yielded usable results. We also simulated three models of the ϵ Eri inner disk using parameters from D. Backman et al. (2009), S. G. Wolff et al. (2023), and S. Ertel et al. (2020), and found that our measurements were over the sensitivity limit predicted by these models. Additionally, using infrared measurements from D. Backman et al. (2009), we have placed an upper limit on the dust albedo, $\omega < 0.487$. JWST observations are likely to resolve the spatial extent of the disk which will better constrain disk parameters for future scattered light observations with observatories such as Roman, which we expect to have a significantly deeper sensitivity limit. The code to reproduce the figures found in this work can be accessed at 10.5281/zenodo.13760813.

Acknowledgments

We thank Schuyler Wolff and András Gáspár for valuable discussions on contrast calculations and consultations on using the AUTOFILET program. We also extend special thanks to Karl Misselt for sharing his expertize in the Fortran programming language in debugging the AUTOFILET program. Additionally, we would like to extend our thanks to Steve Ertel for help with interpreting the HOSTS survey measurements to include in our modeling efforts. We would also like to thank the anonymous referee for their assistance in

[16] https://roman.ipac.caltech.edu/sims/Coronagraph_public_images.html#CGI_OS9
[17] https://roman.ipac.caltech.edu/sims/Coronagraph_public_images.html#Coronagraph_OS11_SPC_Modes

making this a more comprehensive and well rounded piece of work.

Based on observations made with the NASA/ESA Hubble Space Telescope, obtained from the data archive at the Space Telescope Science Institute, which is operated by the Association of Universities for Research in Astronomy, Inc., under NASA contract NAS 5-26555. These observations are associated with program GO 15217. The specific observations analyzed can be accessed can be accessed via DOI:10.17909/gxm6-5x86. STScI is operated by the Association of Universities for Research in Astronomy, Inc. under NASA contract NAS 5-26555. Support for program HST-GO-15217 was provided by NASA through a grant from the Space Telescope Science Institute, which is operated by the Association of Universities for Research in Astronomy, Inc., under NASA contract NAS 5-26555.

Portions of this research were supported by funding from the Technology Research Initiative Fund (TRIF) of the Arizona Board of Regents and by generous anonymous philanthropic donations to the Steward Observatory of the College of Science at the University of Arizona.

This material is based upon High Performance Computing (HPC) resources supported by the University of Arizona TRIF, UITS, and Research, Innovation, and Impact (RII), and maintained by the UArizona Research Technologies department.

Facilities: HST (STIS), Barbara A. Mikulski Archive for Space Telescopes

Software: this research made use of community-developed core Python packages, including Astroquery (A. Ginsburg et al. 2019), Astropy (Astropy Collaboration et al. 2013, 2018, 2022), ccdproc (M. Craig et al. 2017), CuPy (R. Okuta et al. 2017), Matplotlib (J. D. Hunter 2007), NumPy (C. R. Harris et al. 2020), Pandas (W. McKinney 2010; pandas development team 2024), Poppy (M. D. Perrin et al. 2012), PyKLIP (J. J. Wang et al. 2015), centerRadon (B. Ren et al. 2019) SciPy (P. Virtanen et al. 2020), Multiprocess (M. M. McKerns et al. 2012; M. McKerns & M. Aivazis 2010), and the IPython Interactive Computing architecture (F. Perez & B. E. Granger 2007). Additional data analyses were done using IDL (Exelis Visual Information Solutions, Boulder, Colorado). This research has made use of the SIMBAD database, operated at CDS, Strasbourg, France (M. Wenger et al. 2000).

Appendix A
Constraints on Substellar Companions Around ϵ Eri

We used the Sonora Bobcat models (M. S. Marley et al. 2021) considering three different temperatures (500 K, 525 K, and 550 K), and considering solar metallicity with model spectra that fall within the expected age of the ϵ Eri system. We then used the model spectra to determine count rates for the STIS CCD using the Hubble ETC and then calculated contrast. At the highest temperature we considered (550 K), we calculated an upper detection limit on the mass of substellar companions of 8.98 $M_{\rm Jup}$. This corresponds to a contrast of 4.49×10^{-8}, which is slightly less than 6.30×10^{-8}, the contrast we achieve at 1″. We derived this using the planet-focused KLIP reduction, which provides the best absolute contrast at small angular separations. We note that these detection limits do not take into account any reflected light, since that would require assumptions on radius and atmospheric composition that are not known. Since the D. Mawet et al. (2019) observations constrain companion mass to $\sim$1 $M_{\rm Jup}$ at $\sim$1″, a nondetection is not surprising in this case, and even accounting for reflected light would not overcome the order of magnitude difference between prior constraints and our detection limits. Detection limits for three different postprocessing approaches are plotted in Figure 8. A consequence of using standard deviation to calculate contrast is reflected in the Classical RDI plot. Since our data has a larger occurrence of outliers, the sensitivity of standard deviation leads to worse contrast calculations between 1.″5 and 2″.

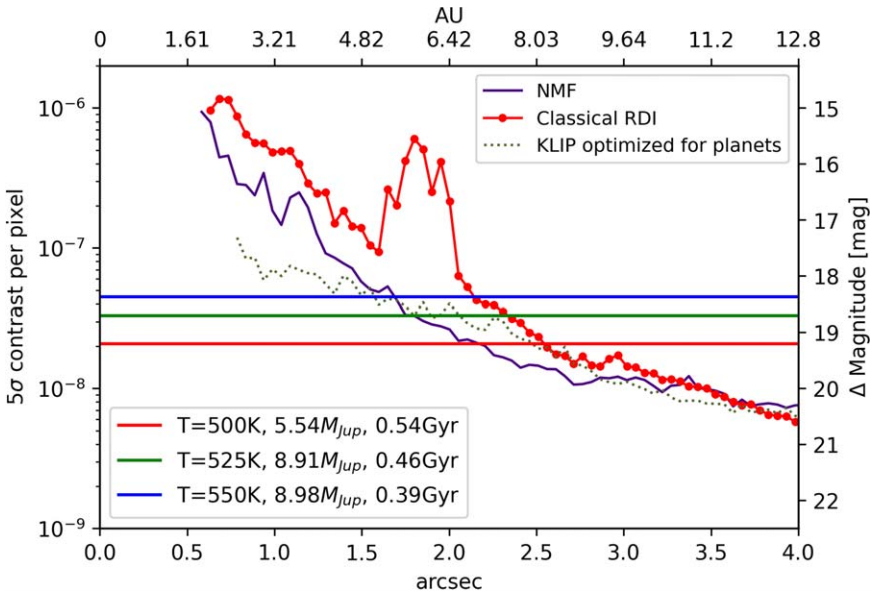

Figure 8. Contrast curves from three different postprocessing approaches plotted against predicted planetary masses (using the Sonora Bobcat planetary evolution models; M. S. Marley et al. 2021) in units of $M_{\rm Jup}$. We use 5σ contrast instead of MAD contrast for this plot to maintain consistency with published exoplanet literature. This plot assumes purely emissive light contrast and does not take reflected light from the planet into effect.

Appendix B
Upper Limits on Disk Flux

To quantify the absolute lowest sensitivity we achieved from our reductions, we measure an upper limit on the radial flux profile of our NMF reduction, which achieved the highest contrast in the region where the inner disk would be, in Figure 9. We present the 1σ uncertainty on the measurement as a shaded region, determined from the noise map used in the creation of the right panel of Figure 2. Consistent with the SNR map of our NMF reduction, our measurement is consistent with a nondetection.

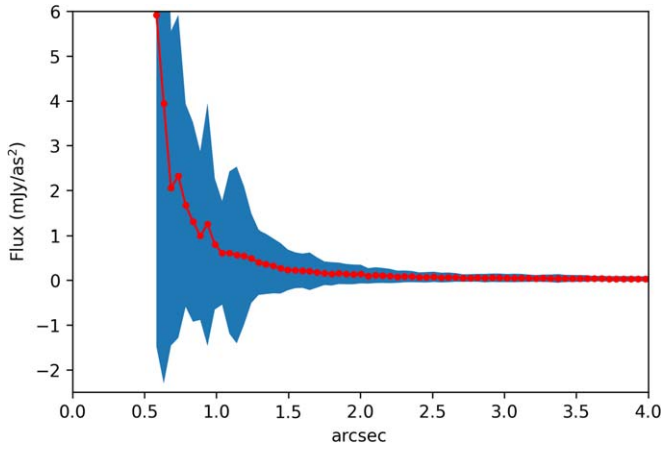

Figure 9. Flux profile of the ϵ Eri system using NMF in red. The shaded blue region represents the 1σ uncertainty in the measurement. Consistent with our derived SNR map, our result is indicative of a nondetection.

ORCID iDs

Sai Krishanth P. M. https://orcid.org/0000-0002-9869-6223
Ewan S. Douglas https://orcid.org/0000-0002-0813-4308
Ramya M. Anche https://orcid.org/0000-0002-4989-6253
Justin Hom https://orcid.org/0000-0001-9994-2142
Kerri L. Cahoy https://orcid.org/0000-0002-7791-5124
John H. Debes https://orcid.org/0000-0002-1783-8817
Hannah Jang-Condell https://orcid.org/0000-0002-7639-1322
Isabel Rebollido https://orcid.org/0000-0002-4388-6417
Bin B. Ren (任彬) https://orcid.org/0000-0003-1698-9696
Yinzi Xin https://orcid.org/0000-0002-6171-9081

References

Amara, A., & Quanz, S. P. 2012, MNRAS, 427, 948
Anche, R. M., Douglas, E., Milani, K., et al. 2023, PASP, 135, 125001
Astropy Collaboration, Price-Whelan, A. M., & Lim, P. L. 2022, ApJ, 935, 167
Astropy Collaboration, Price-Whelan, A. M., & Sipőcz, B. M. 2018, AJ, 156, 123
Astropy Collaboration, Robitaille, T. P., & Tollerud, E. J. 2013, A&A, 558, A33
Aumann, H. H. 1985, PASP, 97, 885
Backman, D., Marengo, M., Stapelfeldt, K., et al. 2009, ApJ, 690, 1522
Backman, D. E., & Paresce, F. 1993, Protostars and Planets III (Tucson, AZ: Univ. Arizona Press), 1253
Ballering, N. P., Su, K. Y. L., Rieke, G. H., & Gáspár, A. 2016, ApJ, 823, 108
Benedict, G. F. 2022, RNAAS, 6, 45
Benedict, G. F., McArthur, B. E., Gatewood, G., et al. 2007, ApJ, 132, 2206
Choquet, E. ´., Bryden, G., Perrin, M. D., et al. 2018, ApJ, 854, 53
Chen, C., Mazoyer, J., Poteet, C. A., et al. 2020, ApJ, 898, 55
Craig, M., Crawford, S., Seifert, M., et al. 2017, astropy/ccdproc: v1.3.0.post1, Zenodo, doi:10.5281/zenodo.1069648
Debes, J. H., Ren, B., & Schneider, G. 2019, JATIS, 5, 035003
Duchêne, G., Rice, M., Hom, J., et al. 2020, AJ, 159, 251
Ertel, S., Defrère, D., Hinz, P., et al. 2020, AJ, 159, 177
Gaia Collaboration, Brown, A. G. A., & Vallenari, A. 2018, A&A, 616, A1
Ginsburg, A., Sipőcz, B. M., Brasseur, C. E., et al. 2019, AJ, 157, 98
Grady, C. A., Proffitt, C. R., Malumuth, E. M., et al. 2003, PASP, 115, 1036
Greaves, J. S., Holland, W. S., Moriarty-Schieven, G., et al. 1998, ApJL, 506, L133
Harris, C. R., Millman, K. J., van der Walt, S. J., et al. 2020, Natur, 585, 357
Hatzes, A. P., Cochran, W. D., McArthur, B., et al. 2000, ApJL, 544, L145
Howard, A. W., & Fulton, B. J. 2016, PASP, 128, 114401
Hunter, J. D. 2007, CSE, 9, 90
Hunziker, S., Schmid, H. M., Mouillet, D., et al. 2020, A&A, 634, A69
Hurt, S. A., & MacGregor, M. A. 2023, ApJ, 954, 10
Jansen, R. A., Collins, N. R., & Windhorst, R. A. 2003, in HST Calibration Workshop: Hubble after the Installation of the ACS and the NICMOS Cooling System, ed. S. Arribas et al. (Baltimore, MD: STSI), 193
Kasdin, N. J., Bailey, V. P., Mennesson, B., et al. 2020, Proc. SPIE, 11443, 114431U
Llop-Sayson, J., Wang, J. J., Ruffio, J.-B., et al. 2021, AJ, 162, 181
MacGregor, M. A., Wilner, D. J., Andrews, S. M., et al. 2015, ApJ, 809, 47
Marley, M. S., Saumon, D., Visscher, C., et al. 2021, ApJ, 920, 85
Mawet, D., Hirsch, L., Lee, E. J., et al. 2019, AJ, 157, 33
McKerns, M., & Aivazis, M. 2010, pathos: a framework for heterogeneous computing, https://mmckerns.github.io/project/pathos/wiki.html
McKerns, M. M., Strand, L., Sullivan, T., et al. 2012, arXiv:1202.1056
McKinney, W. 2010, in Proc. 9th Python in Science Conf. (Austin, TX: SciPy), 51
Nemati, B., Shao, M., Gonzalez, G., et al. 2020, Proc. SPIE, 11443, 114430O
Okuta, R., Unno, Y., Nishino, D., et al. 2017, in 31st Conf. Neural Information Processing Systems (NIPS 2017) (Long Beach, CA: NIPS), 1, http://learningsys.org/nips17/assets/papers/paper_16.pdf
pandas development team 2024, pandas-dev/pandas: Pandas, v.2.2.2, Zenodo, doi:10.5281/zenodo.10957263
Perez, F., & Granger, B. E. 2007, CSE, 9, 21
Perrin, M. D., Soummer, R., Elliott, E. M., et al. 2012, Proc. SPIE, 8442, 84423D
Pickles, A. J. 1998, PASP, 110, 863
Pinte, C., Ménard, F., Duchêne, G., & Bastien, P. 2006, A&A, 459, 797
Poberezhskiy, I., Heydorff, K., Luchik, T., et al. 2022, Proc. SPIE, 12180, 121801X
Poberezhskiy, I., Luchik, T., Zhao, F., et al. 2021, Proc. SPIE, 11443, 114431V
Proffitt, C. R., Sahu, K., Livio, M., et al. 2004, ApJ, 612, 481
Ren, B., Pueyo, L., Perrin, M. D., et al. 2017, Proc. SPIE, 10400, 1040021
Ren, B., Pueyo, L., Zhu, G. B., et al. 2018, ApJ, 852, 104
Ren, B., Wang, J. J., & Pueyo, L., 2019 centerRadon: Center determination code in stellar images, Astrophysics Source Code Library, ascl:1906.021
Sai Krishanth, P. M., Douglas, E. S., & Hom, J. 2023, Proc. SPIE, 12680, 1268021
Schneider, G., Grady, C. A., Hines, D. C., et al. 2014, AJ, 148, 59
Soummer, R., Pueyo, L., & Larkin, J. 2012, ApJL, 755, L28
Su, K. Y. L., De Buizer, J. M., Rieke, G. H., et al. 2017, AJ, 153, 226
Virtanen, P., Gommers, R., Oliphant, T. E., et al. 2020, NatMe, 17, 261
Wang, J. J., Ruffio, J.-B., De Rosa, R. J., et al., 2015 pyKLIP: PSF Subtraction for Exoplanets and Disks, Astrophysics Source Code Library, ascl:1506.001
Wenger, M., Ochsenbein, F., Egret, D., et al. 2000, A&AS, 143, 9
Wolff, S. G., Gáspár, A., H. Rieke, G., et al. 2023, AJ, 165, 115
Xie, C., Choquet, E., Vigan, A., et al. 2022, A&A, 666, A32
Ygouf, M., Zimmerman, N., Bailey, V., et al. 2021, AAS Meeting, 53, 332.05